

Phenomenology of Andreev reflection from first-principles transport theory

Awadhesh Narayan, Ivan Rungger, and Stefano Sanvito

School of Physics, AMBER and CRANN Institute, Trinity College, Dublin 2, Ireland

(Dated: August 24, 2021)

We study Andreev reflection in normal metal-superconductor junctions by using an extended Blonder-Tinkham-Klapwijk model combined with transport calculations based on density functional theory. Starting from a parameter-free description of the underlying electronic structure, we perform a detailed investigation of normal metal-superconductor junctions, as the separation between the superconductor and the normal metal is varied. The results are interpreted by means of transverse momentum resolved calculations, which allow us to examine the contributions arising from different regions of the Brillouin zone. Furthermore we investigate the effect of a voltage bias on the normal metal-superconductor conductance spectra. Finally, we consider Andreev reflection in carbon nanotubes sandwiched between normal and superconducting electrodes.

PACS numbers:

I. INTRODUCTION

An electron incident on a superconductor from a normal metal, with an energy smaller than the superconducting energy gap, cannot propagate into the superconductor and thus should be perfectly reflected. However, Andreev discovered a mechanism for transmission, in which an electron may form a Cooper pair with another electron and be transmitted across the superconductor. As a consequence of charge conservation a hole must be left behind, which, as a result of momentum conservation, should propagate in a direction opposite to that of the incident electron. This process is termed Andreev reflection¹.

Apart from providing a confirmation for the existence of Cooper pairs and superconductor energy gaps², this process may also have applications in spintronics. It has been suggested that point contact Andreev reflection can be used to probe spin polarization of ferromagnets by fabricating ferromagnet-superconductor nanojunctions^{3,4}. Materials-specific modelling of such experiments, however, is complex and so far it has been somewhat unsatisfactory. For instance tight-binding based scattering theory⁵ and Green's functions theory⁶ calculations found poor fits to the experimental data for ferromagnet-superconductor junctions, while produced excellent fitting to normal metal-superconductor junctions results. Based on this observation, Xia and co-workers suggested that there may be an interaction between the ferromagnet and superconductor which is not accounted for in the Blonder-Tinkham-Klapwijk (BTK) model⁶. Consequently, the simple interpretation and two-parameter BTK model fitting of experimental data to extract the spin polarization of various ferromagnets, was also called into question. More recently, Chen, Tesanovic and Chien proposed a unified model for Andreev reflection at a ferromagnet-superconductor interface⁷. This is based on a partially polarized current, where the Andreev reflection is limited by minority states and the excess majority carriers provide an evanescent contribution. However, this model has also been called

into doubt by Eschrig and co-workers⁸. In particular, they pointed out that the additional evanescent component is introduced in an *ad-hoc* manner, and that the resulting wavefunction violates charge conservation. So, the debate about the correct model to describe Andreev reflection at a ferromagnet-superconductor junction seems far from being settled.

Among other mesoscopic systems, Andreev reflection has also been measured in carbon nanotubes (CNTs)⁹. There has been a theoretical study of normal metal-molecule-superconductor junction from density functional theory based transport calculations¹⁰. In this study it was shown that the presence of side groups in the molecule can lead to Fano resonances in Andreev reflection spectra. Topological insulators, a very recent and exciting development in condensed matter physics, have also been shown to be characterized by perfect Andreev reflection¹¹⁻¹⁴.

Wang and co-authors have recently suggested performing a self-consistent calculation of the scattering potential to study Andreev reflection at normal metal-superconductor junctions¹⁵. They calculated the conductance for carbon chains sandwiched between a normal and a superconducting Al electrode and found different values depending on whether or not the calculation was carried out self-consistent over the Hartree and exchange-correlation potential. However, the theoretical justification for such a self-consistent procedure is at present not clear. In particular, it is difficult to argue that the variational principle, which underpins the Hohenberg-Kohn theorems, is still obeyed when a pairing energy is added *by hand* to the Kohn-Sham potential. In principle a rigorous self-consistent treatment should use the superconducting version of density functional theory¹⁶, which probably remains computationally too expensive for calculating the interfaces needed to address a scattering problem. Given such theoretical landscape and the fact that a non self-consistent approach to density functional theory based transport calculations has shown excellent agreement to experimental results for normal metal-superconductor junctions, we follow this

methodology in the present work.

In this paper, we study Andreev reflection in normal-superconductor junctions, including all-metal junctions and carbon nanotubes sandwiched between normal and superconducting electrodes. We take into account the atomistic details of the junction by using density functional theory to obtain the underlying electronic structure, and then employ an extended BTK model to solve the normal-superconductor scattering problem. Our transverse momentum resolved calculations allow identifying the contributions to conductance from different parts of the Brillouin zone. We also study the variation of conductance as a function of an applied potential difference between the electrodes for various normal metal-superconductor junctions, by performing approximate finite bias calculations.

After this introduction, the rest of our paper is organized as follows: in Section II we summarize the extended BTK model and Beenakker's formula, which we employ in this work. In the subsequent Section III, we present our results for Cu-Pb, Co-Pb and Au-Al junctions, as well as Al-CNT-Al junctions. We also include the computational details in each of these subsections. Finally, we conclude and summarize our findings in Section IV.

II. FORMULATION

For the sake of completeness, here we briefly summarize the extended BTK model¹⁸ that we use to study Andreev reflection at a normal metal-superconductor interface. Following Refs. [6,17], we begin with the Bogoliubov-de Gennes equation

$$\begin{pmatrix} H_\sigma & \Delta e^{i\phi} \\ \Delta^* e^{-i\phi} & -H_{-\sigma}^* \end{pmatrix} \begin{pmatrix} \psi_{e\sigma} \\ \psi_{h-\sigma} \end{pmatrix} = \varepsilon \begin{pmatrix} \psi_{e\sigma} \\ \psi_{h-\sigma} \end{pmatrix}, \quad (1)$$

where H_σ is the single particle Hamiltonian for majority ($\sigma = 1$) and minority ($\sigma = -1$) spins, Δ is the pairing potential and ψ_e and ψ_h are respectively the electron and hole wavefunctions. The energy $\varepsilon = E - E_F$ sets the reference to the Fermi energy, E_F . We follow the approach of Beenakker consisting in inserting a layer of superconductor in its normal state between the metal-superconductor interface. This ensures that at the fictitious normal metal-superconductor interface the only scattering process is Andreev scattering.

Other scattering processes are accounted for at the junction between the normal metal and superconductor in its normal state. At this interface the scattering matrix can be written as

$$\begin{pmatrix} \psi_{1,e\sigma}^- \\ \psi_{2,e\sigma}^+ \\ \psi_{1,h-\sigma}^+ \\ \psi_{2,h-\sigma}^- \end{pmatrix} = \begin{pmatrix} s^\sigma(\varepsilon) & 0 \\ 0 & s^{-\sigma*}(-\varepsilon) \end{pmatrix} \begin{pmatrix} \psi_{1,e\sigma}^+ \\ \psi_{2,e\sigma}^- \\ \psi_{1,h-\sigma}^- \\ \psi_{2,h-\sigma}^+ \end{pmatrix}. \quad (2)$$

Here the superscripts + and - denote the right- and left-going states and the subscripts 1 and 2 refer to the

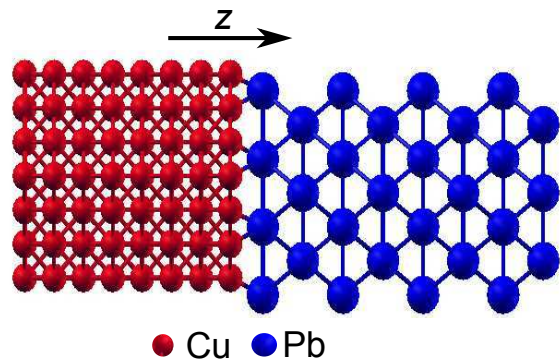


FIG. 1: (Color online) Scattering region for a Cu-Pb junction. Transport calculations are performed for different distances between Cu and Pb, employing periodic boundary conditions in the plane normal to the transport direction, z , indicated by the arrow. Self-energies are used to simulate the effect of semi-infinite leads attached to the edge of the scattering region.

normal and fictitious normal metal regions, respectively. The normal state scattering matrix reads

$$s^\sigma(\varepsilon) = \begin{pmatrix} r_{11}^\sigma & t_{12}^\sigma \\ t_{21}^\sigma & r_{22}^\sigma \end{pmatrix}. \quad (3)$$

Now at the fictitious normal metal-superconductor interface

$$\psi_{2,e\sigma}^- = \alpha \psi_{2,h-\sigma}^- e^{i\phi}, \quad \psi_{2,h-\sigma}^+ = \alpha^* \psi_{2,e\sigma}^+ e^{-i\phi}, \quad (4)$$

where the factor α is

$$\begin{aligned} \alpha &= \exp[-i \cos^{-1}(\varepsilon/\Delta)], \quad |\varepsilon| < \Delta \\ &= \frac{1}{\Delta}[\varepsilon - \text{sign}(\varepsilon)\sqrt{\varepsilon^2 - \Delta^2}], \quad |\varepsilon| > \Delta. \end{aligned} \quad (5)$$

The states in the normal metal are given by

$$\begin{pmatrix} \psi_{1,e\sigma}^- \\ \psi_{1,h-\sigma}^+ \end{pmatrix} = \begin{pmatrix} R_{ee}^\sigma & R_{eh}^\sigma \\ R_{he}^\sigma & R_{hh}^\sigma \end{pmatrix} \begin{pmatrix} \psi_{1,e\sigma}^+ \\ \psi_{1,h-\sigma}^- \end{pmatrix}. \quad (6)$$

Then the reflection coefficients for the complete system are

$$R_{ee}^\sigma = r_{11}^\sigma(\varepsilon) + \alpha^2 t_{12}^\sigma(\varepsilon) r_{22}^{-\sigma*}(-\varepsilon) \frac{1}{1 - \alpha^2 r_{22}^\sigma(\varepsilon) r_{22}^{-\sigma*}(-\varepsilon)} t_{21}^\sigma(\varepsilon), \quad (7)$$

and

$$R_{he}^\sigma = \alpha^* e^{-i\phi} t_{12}^{-\sigma*}(-\varepsilon) \frac{1}{1 - \alpha^2 r_{22}^\sigma(\varepsilon) r_{22}^{-\sigma*}(-\varepsilon)} t_{21}^\sigma(\varepsilon). \quad (8)$$

Finally the conductance of the system is given by

$$G_{NS}(\varepsilon) = \frac{e^2}{h} \sum_{\sigma=\pm 1} \text{Tr}(1 - R_{ee}^\sigma R_{ee}^{\sigma\dagger} + R_{he}^\sigma R_{he}^{\sigma\dagger}). \quad (9)$$

The implicit assumptions in the above derivation are that the superconducting order parameter is switched on

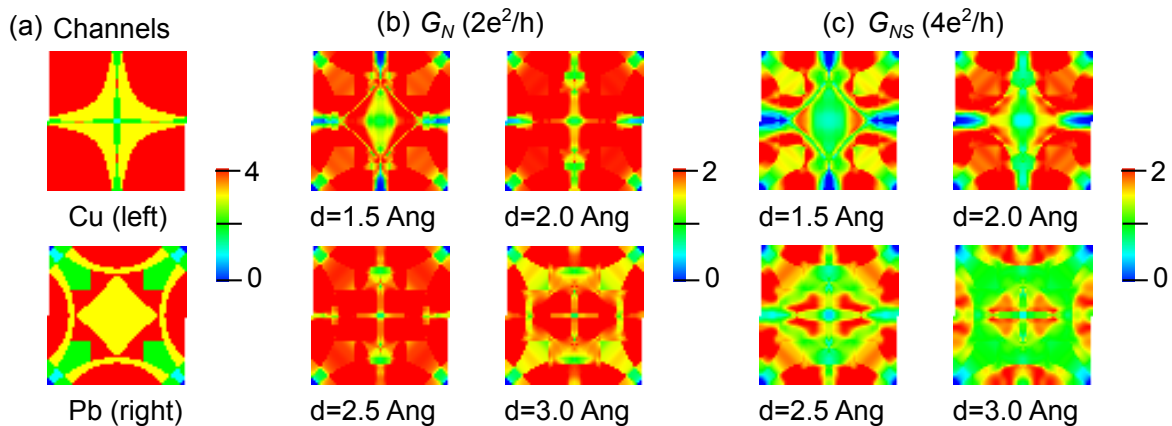


FIG. 2: (Color online) Cu-Pb junction: k -resolved transport quantities at the Fermi level. (a) A $k_x - k_y$ resolved plot of the channels in the left-hand (Cu) and right-hand side (Pb) electrodes. (b) Normal conductance, G_N , and (c) normal metal-superconductor conductance, G_{NS} , plotted across the Brillouin zone at different Cu-Pb separations, d , ranging from 1.5 Å to 3.0 Å.

abruptly as a step function (i.e., there are no proximity effects) and the order parameter is much smaller than the Fermi energy (the so-called Andreev approximation).

A great simplification occurs if one considers scattering at Fermi energy, namely $\varepsilon = 0$, and the presence of time reversal symmetry, i.e., the normal metal is not a ferromagnet. The above expression for conductance reduces to

$$G_{NS}(\varepsilon = 0) = \frac{4e^2}{h} \text{Tr} \left(\frac{t_{12}t_{12}^\dagger}{2 - t_{12}t_{12}^\dagger} \right)^2 = \frac{4e^2}{h} \sum_n \frac{T_n^2}{(2 - T_n)^2}, \quad (10)$$

where the eigenvalues of the transmission matrix product $t_{12}t_{12}^\dagger$ are T_n . This is the Beenakker's formula¹⁹. Notice that all the dependence on the superconductor pairing has dropped out and the conductance depends on the normal state transmission eigenvalues. In this case superconductivity enters implicitly in the form of a boundary condition. In our first-principles transport code SMEAGOL²⁰⁻²², we construct the full scattering matrix and then use the expressions in equations (7) and (8) to evaluate the conductance from equation (9). For the special case of $\varepsilon = E - E_F = 0$, we construct the transmission matrix, $t_{12}t_{12}^\dagger$. It is then straightforward to obtain its eigenvalues by numerical diagonalization. These are then inserted into the Beenakker's formula [equation (10)] to obtain G_{NS} , while a direct summation of the eigenvalues yields $G_N = \frac{2e^2}{h} \sum_n T_n$. To compute the current, I , at a bias V , we use G_{NS} from equation (9) and calculate

$$I(V) = \frac{1}{e} \int d\varepsilon [f(\varepsilon) - f(\varepsilon + eV)] G(\varepsilon), \quad (11)$$

and the finite bias conductance is evaluated from

$$G(V) = \int d\varepsilon \left(-\frac{\partial f}{\partial \varepsilon} \right) G(\varepsilon). \quad (12)$$

Here G can either be the normal state conductance, G_N , or the normal metal-superconductor conductance, G_{NS} , and f is the Fermi function.

III. RESULTS

A. Cu-Pb junction

We begin by presenting our results for Cu-Pb junctions, which have also been investigated experimentally in the past³. We choose Cu $3d$ and $4s$ and Pb $6s$ and $6p$ as valence electrons and the effect of other core electrons are described by Troullier-Martins norm-conserving pseudopotentials. The local density approximation with the Ceperley-Alder parametrization was employed for the exchange-correlation functional. We choose an energy cutoff of 400 Rydberg for the real space mesh, and a double- ζ polarized basis set. The lattice constants of Cu ($a = 3.615$ Å) and Pb ($a = 4.93$ Å) are quite different, however a matching is obtained by rotating Cu unit cell by a 45° angle. In this geometry a small strain ($\approx 2\%$) exists on both Cu (compressive) and Pb (tensile). For the self-consistent calculation we use a 4×4 in plane Monkhorst-Pack grid, while transport quantities are evaluated over a much denser 60×60 k grid.

The scattering region for a Cu-Pb junction is shown in Fig. 1. We use periodic boundary conditions in the plane orthogonal to the transport direction, and open boundary conditions along the direction of transport. We plot the available channels for both electrodes resolved over the Brillouin zone (BZ) at the Fermi energy in Fig. 2(a). For the left electrode (Cu) four channels are available in quadrants centered at the edge of the BZ, with a residual region around the zone center in which either three or two channels are available. For the right electrode (Pb) around the BZ center there exists a rectangular region

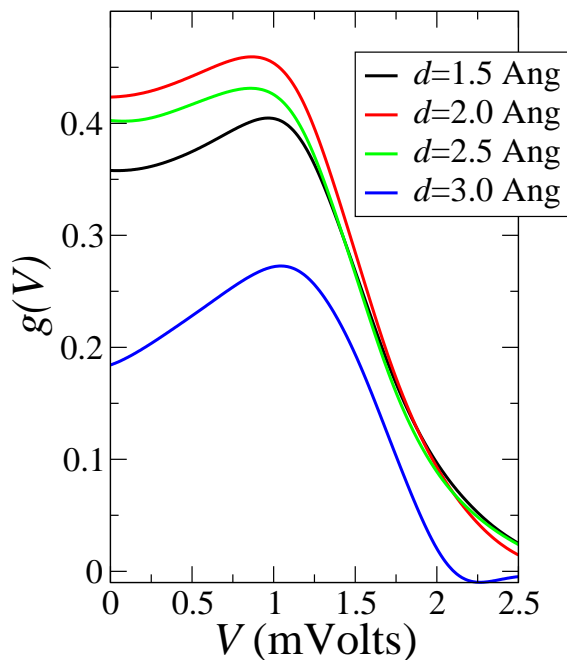


FIG. 3: (Color online) Normalized conductance at finite bias for Cu-Pb junction at different distances, d , between Cu and Pb. Note that $g(V = 0)$ remains positive for all the distances investigated here.

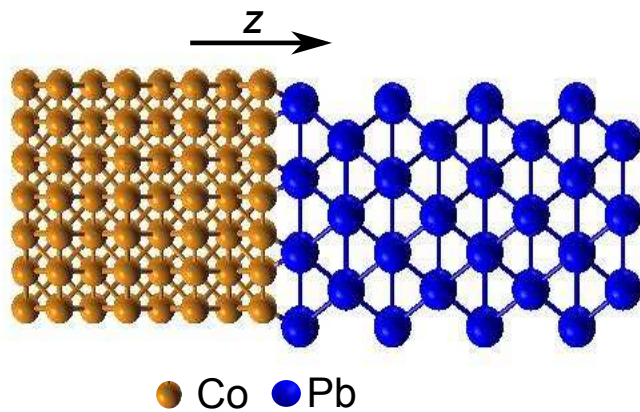


FIG. 4: (Color online) Scattering region for the Co-Pb junction. Semi-infinite Co and Pb leads are attached to the left-hand and right-hand side ends of the junction, respectively. In the $x - y$ plane (orthogonal to transport direction, z) periodic boundary conditions are employed.

with three open channels, while at the BZ corners there are small pockets of reduced available channels, which even drop down to zero. The normal conductance, G_N , is large over almost the entire BZ, along with small pockets of lower transmission at the edges of the BZ, which are inherited from the reduced channel pockets in the Pb electrode, as shown in Fig. 2(b). Another small conductance pocket is present at the zone center, which origi-

nates from the distribution of open channels across the BZ in the Cu electrode.

The overall conductance remains largely unchanged as the Cu-Pb distance is increased from $d = 1.5$ to 3.0 Å. Next we show the normal metal-superconductor junction conductance, G_{NS} , in Fig. 2(c). At $d = 1.5$ Å, the pockets of small conductance at the zone edges are more prominent, as compared to G_N . Moreover, the region around $k_x = k_y = 0$, with reduced conductance is also larger. On increasing the distance to 2 Å, these low conductance pockets shrink in size and the overall conductance increases. At larger distances, a broader region of low conductance develops and this reduces overall G_{NS} . In Table I, we provide the k -averaged value of the conductance above (G_N) and below (G_{NS}) the Pb superconducting temperature. For both quantities a maximum is obtained at $d = 2$ Å. We also tabulate the ratio G_{NS}/G_N , which is the quantity expressing the zero-bias suppression due to Andreev reflection. For a single channel BTK model describing an ideal interface this ratio is exactly two, however when one takes into account the band structure mismatch and the underlying electronic structure of the electrodes a much lower value for this ratio can be obtained. For the Cu-Pb equilibrium distance ($d \approx 2.0$ Å) we find G_{NS}/G_N close to 1.4, which is in excellent agreement with the experimental value of 1.38 reported in Ref. 3.

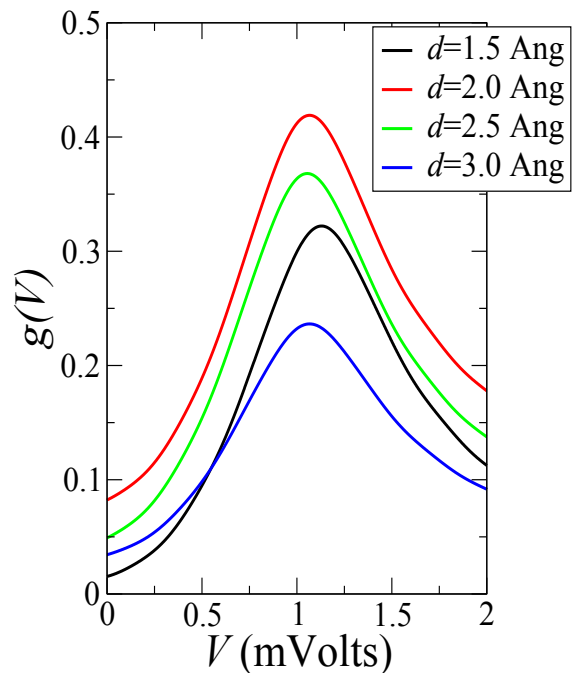


FIG. 5: (Color online) Normalized conductance at finite bias for a Co-Pb junction at different distances, d , between the two constituents.

We also calculate the conductances at finite bias, for which we use the bulk Pb superconducting gap, $\Delta = 1.36$

TABLE I: Cu-Pb junction: Normal conductance, G_N , normal-superconductor conductance, G_{NS} , and their ratio at different Cu/Pb distances.

Distance (\AA)	$G_N(2e^2/h)$	$G_{NS}(2e^2/h)$	G_{NS}/G_N
1.5	2.097	2.847	1.358
2.0	2.291	3.261	1.423
2.5	2.263	3.173	1.402
3.0	1.957	2.318	1.184

meV, and a temperature of 4.2 K in the Fermi distribution. The normalized conductance, $g(V)$, which is the quantity suitable for comparison across experiments, reads

$$g(V) = \frac{G_{NS}(V) - G_N(V)}{G_N(0)}, \quad (13)$$

where $G_{NS}(V)$ is the conductance at finite bias and temperature. Fig. 3 shows $g(V)$ at different distances between the superconducting tip and the substrate. By large all the $g(V)$ curves follow a similar trend. They do start in the range $[0.2, 0.4]$ for zero bias voltage, then they increase as the applied voltage gets larger. A maximum is achieved for V close to the superconducting gap, and then $g(V)$ decreases for higher bias, since there is no Andreev reflection for energies above the superconducting gap. The normalized conductance curves for $d = 1.5, 2.0$ and 2.5 \AA are quite closely spaced, while a considerable drop is seen for $d = 3.0 \text{ \AA}$. However, for small bias voltages of upto 2 mV, the normalized conductance remains positive, i.e., $G_{NS} > G_N$, for all distances to 3 \AA . This is consistent with experiments³.

B. Co-Pb junction

Next, we present our results for Co-Pb junctions. We choose Co $3d$ and $4s$ and Pb $6s$ and $6p$ as valence electrons, while the core electrons are described by Troullier-Martins norm-conserving pseudopotentials. As in the Cu-Pb case, the local density approximation with the Ceperley-Alder parametrization was employed for the exchange-correlation functional and an energy cutoff of 400 Rydberg was chosen for the real space mesh. We selected a double- ζ polarized basis set. Similarly to the case of the Cu-Pb junction, we face the issue that the Co ($a = 3.548 \text{ \AA}$) and Pb ($a = 4.93 \text{ \AA}$) lattice constants are quite different. Once again, we obtain a good lattice match by rotating the Co unit cell by a 45° angle, and the scattering region setup is shown in Fig. 4. A 4×4 in plane Monkhorst-Pack grid k -point sampling was used for the self-consistent calculation, and the transport quantities were evaluated over a dense 60×60 k -grid. Note that Co is ferromagnetic and its spin polarization was determined based on a fit to the two parameter BTK model in Refs. [3,4].

The zero bias conductances, G_N and G_{NS} , along with their ratio is presented in Table II. There is a small variation of both G_N and G_{NS} as the substrate-superconducting tip distance, d , is changed. We note that the ratio G_{NS}/G_N is reduced (to values close to one), in comparison to the Cu-Pb case. This is a manifestation of the ferromagnetism, where only one spin channel dominates around the Fermi level. As a consequence Andreev reflection is suppressed, since there are no opposite spin channels available for the hole and this hinders the formation of the Cooper pair in the superconductor. The values of this ratio obtained from our calculations are in good agreement with experimental studies³, as well as previous calculations^{5,6}.

The apparent match between experiments and theory is lost once one considers a finite bias situation. This can be appreciated in Fig. 5, where we plot the normalized conductance, $g(V)$, for different d . For all the distances investigated, $g(V)$ presents a similar shape. The curves start from a small value comprised between 0 and 0.1 around zero bias. They then increase and reach a maximum at around 1.3 mV. The main noticeable feature is the strong enhancement of $g(V)$, i.e., an increased Andreev reflection, at voltages close to the superconducting gap edge. Our results match previous calculations by Xia *et al.*⁶, but they do not fit well the measurements of Upadhyay *et al.* [3]. In fact, in actual samples such strong enhancement of $g(V)$ near the superconductor gap edge is not seen. This discrepancy was attributed to the possibility of stray fields from the ferromagnet, which can cause spin-dependent splitting of the superconductor density of states⁶. Other possible reasons may include proximity effects, which are not taken into account in the extended BTK model and require a full DFT description of the superconducting state across the junction.

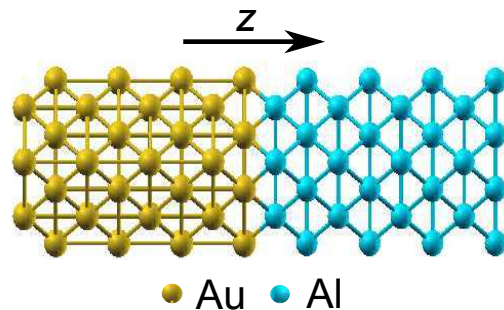


FIG. 6: (Color online) Scattering region for an Au-Al junction. Au and Al semi-infinite leads are attached to the left-hand and right-hand side ends of the junction, respectively. Periodic boundary conditions are used in the plane perpendicular to the transport direction, z .

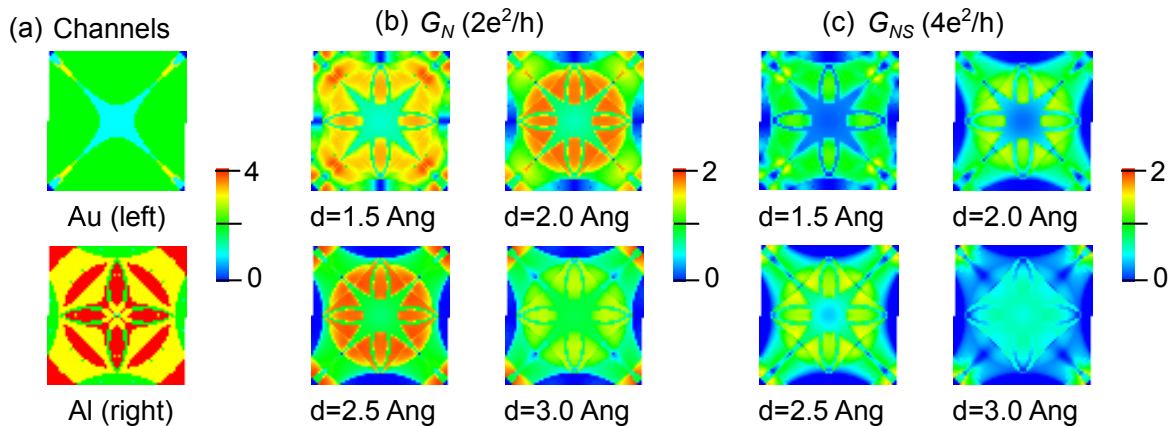


FIG. 7: (Color online) Au-Al junction: k -resolved transport quantities at the Fermi level. (a) A $k_x - k_y$ plot of the number of channels available in the left-hand side Au electrode (top panel) and the right-hand side Al electrode (bottom panel). (b) Normal conductance (G_N) across the junction plotted across the Brillouin zone orthogonal to the transport direction at different Al/Au distances, d , in its normal state. (c) A $k_x - k_y$ resolved plot of the normal metal-superconductor conductance (G_{NS}) at different d . Note the same scale on the color plots for G_N and G_{NS} , while different units are used for the two conductances.

TABLE II: Co-Pb junction: Normal conductance, G_N , normal-superconductor conductance, G_{NS} , and their ratio at different Co/Pb distances.

Distance (\AA)	$G_N(2e^2/h)$	$G_{NS}(2e^2/h)$	G_{NS}/G_N
1.5	1.659	1.679	1.012
2.0	1.668	1.803	1.081
2.5	1.627	1.705	1.048
3.0	1.539	1.588	1.032

C. Au-Al junction

Next, we move on to Au-Al junctions. We considered Au $5d$ and $6s$ and Al $3s$ and $3p$ as valence electrons and the core electrons are described again by Troullier-Martins norm-conserving pseudopotentials. Similarly to the case of the Cu-Pb junction, the local density approximation with the Ceperley-Alder parametrization is employed for the exchange-correlation functional. We choose an energy cutoff of 400 Rydberg for the real space mesh, and a double- ζ polarized basis set. Since the lattice constants of Au ($a = 4.078\text{\AA}$) and Al ($a = 4.037\text{\AA}$) are quite close, a matching Au-Al junction is constructed with a small strain of $\approx 1\%$ on Au. For the self-consistent calculation, we used a 4×4 in plane Monkhorst-Pack grid. From this converged density, the various transport quantities are evaluated using a 60×60 k -point grid.

The scattering setup is shown in Fig. 6, with transport along the z direction. Similarly to the Cu-Pb junction, we use periodic boundary conditions in the plane perpendicular to the transport direction and attach self-energies corresponding to semi-infinite Au and Al on the left-hand and right-hand sides, respectively. The k -resolved quantities are presented in Fig. 7. Over most of the BZ, two

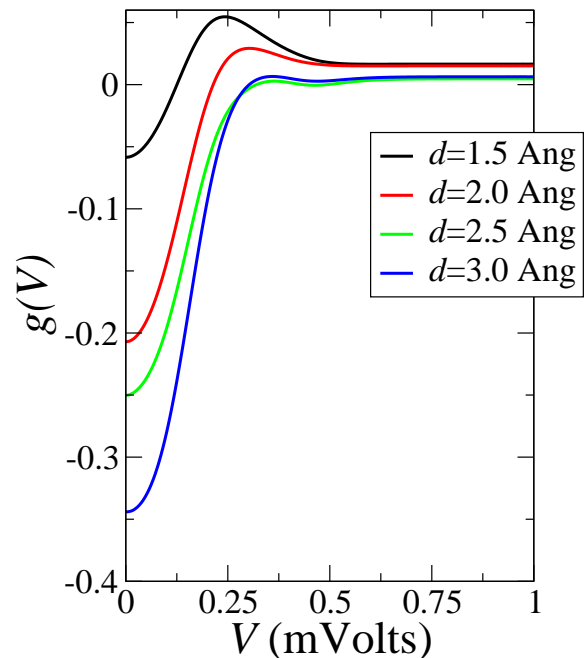


FIG. 8: (Color online) Normalized conductance at finite bias for a Au-Al junction at different Au/Al distances, d .

channels are available for the Au electrode, which reduces to a single channel around the zone center ($k_x = k_y = 0$). The Al electrode, in contrast, provides a minimum of two channels over the entire BZ. The normal conductance G_N (i.e. the conductance of the junction when the temperature is greater than the critical superconducting temperature for Al), is shown in Fig. 7(b) for different distances between Au and Al.

The qualitative picture obtained for the four distances

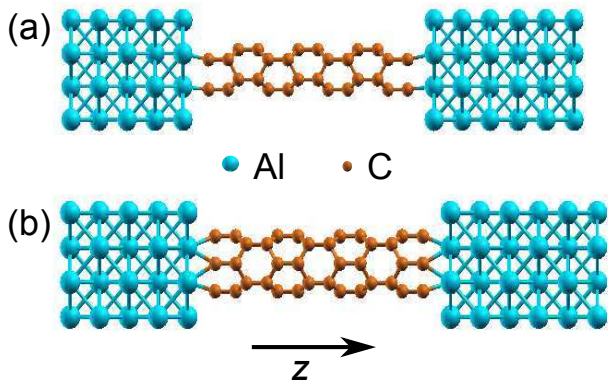


FIG. 9: (Color online) Scattering region for (a) Al-CNT(3,0)-Al and (b) Al-CNT(4,0)-Al junctions. In these two cases the same Al leads are attached on both sides of the scattering region.

investigated in this work is similar. There is a four-fold symmetric feature at the zone center, which originates from the available states in the Au electrode. Around this central feature, a circular maximum in conductance is seen. This resembles the k distribution of channels in the Al electrode. Its intensity increases as one goes from a distance of 1.5 Å to 2.5 Å, but subsequently falls at $d=3$ Å. In Fig. 7(c) we plot the normal metal-superconductor conductance G_{NS} of the Au-Al junction. In this case, as for G_N , the four-fold symmetric feature arising from Au channels is seen around the BZ center. However, at $d=2$ and 2.5 Å, a circular region with reduced conductance value develops around $k_x = k_y = 0$. Furthermore, the circular feature in the normal conductance, obtained from the channels in Al electrode, takes a more dispersed shape in G_{NS} . Yet, the general trend that this region contributes most to the conductance remains. The values of G_N and G_{NS} averaged over the entire BZ, for different distances, are summarized in Table III. For all the four distances investigated, G_N remains close to around one quantum of conductance, while it decreases as the distance between Au and Al is increased. Following a similar trend, G_{NS} also decreases with increasing separation. In this case of a Au-Al junction the ratio G_{NS}/G_N is obtained to be smaller than unity for all the four distances, in contrast to Cu-Pb junctions. This means that for Au-Al junctions the normal state conductance is larger than the superconducting state conductance. This provides a stark contrast to the expectation of doubling the conductance upon switching on superconductivity provided by the BTK model. Our results also emphasize the importance of taking into account the electronic structure of the materials forming the junction, as well as the Fermi surface mismatch between them.

Finally in Fig. 8 we plot the normalized conductance for different Au-Al separations. The superconducting gap for Al is $\Delta = 0.17$ meV and we select a temperature of 1.2 K in the Fermi distribution. In contrast to

TABLE III: Au-Al junction: Normal conductance, G_N , normal-superconductor conductance, G_{NS} , and their ratio at different Au/Al distances.

Distance (Å)	$G_N(2e^2/h)$	$G_{NS}(2e^2/h)$	G_{NS}/G_N
1.5	1.232	1.161	0.942
2.0	1.146	0.909	0.793
2.5	1.074	0.806	0.751
3.0	0.858	0.563	0.656

the previous two junctions, in this case $g(V)$ is negative at low bias, since G_{NS} is smaller than G_N . Furthermore, in this small bias regime increasing d leads to a reduction in the value of the normalized conductance. For larger bias values, $g(V)$ rises as the voltage bias is increased and G_{NS} and G_N become almost equal and the normalized conductance tends to zero.

D. Al-CNT-Al junctions

We now discuss our investigation of Al-CNT-Al junctions. We select Al 3s and 3p and C 2s and 2p as valence electrons, and again norm-conserving pseudopotentials describe the core electrons. As before, we choose the local density approximation to the exchange-correlation functional, a real space mesh cutoff of 400 Rydberg and a double- ζ polarized basis set. We use a 4×4 in plane k -point grid transverse to transport direction both for converging the charge density and for evaluating the conductances.

We study (3,0) and (4,0) CNTs sandwiched between Al electrodes and we assume that one of them can be turned into a superconductor below a critical temperature. In practice this may be achieved by a proximity effect with a superconductor with a higher critical temperature, for example Sn, Pb or Nb. We fix the distance between the CNTs and the Al surface to 2 Å, and the CNT is left open-ended. The scattering region setup for the two cases is shown in Fig. 9. We have checked that the number of available states in Al leads is at least eight over the entire BZ. For Al-CNT(3,0)-Al junction, the major contribution to the normal conductance, G_N , comes from the zone center. A similar feature is seen for Al-CNT(4,0)-Al junction, where the conductance is dominated by the BZ center. The normal-superconductor conductance, G_{NS} , presents a very similar BZ picture for both types of CNTs. The k -averaged values are summarized in Table IV. The conductance values for the two CNTs are found to be similar. Interestingly, we find the ratio G_{NS}/G_N to lie on opposite sides of unity; for (3,0) CNT it is above one, while it falls below one for (4,0) junction. This is reminiscent of the even-odd effect in C wires sandwiched between Al superconducting electrodes. Wang *et al.* found that the zero bias Andreev conductance oscillates as the number of C atoms

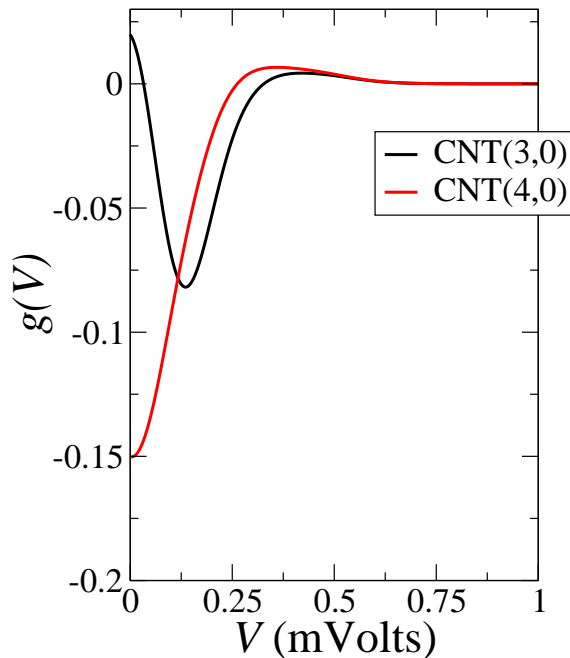


FIG. 10: (Color online) Normalized conductance at finite bias for Al-CNT-Al junctions. For CNT(3,0) $g(V)$ starts from a positive value and changes sign with the applied bias, while for the case of CNT(4,0) it remains negative.

is changed from even to odd¹⁵.

TABLE IV: Al-CNT-Al junction: Normal conductance (G_N), normal-superconductor conductance (G_{NS}) and their ratio for different CNT's.

CNT	$G_N(2e^2/h)$	$G_{NS}(2e^2/h)$	G_{NS}/G_N
(3,0)	1.362	1.389	1.020
(4,0)	1.431	1.217	0.850

Finally, we study the variation of normalized conductance as a function of an applied bias, which is plotted in Fig. 10. At low bias, for Al-CNT(3,0)-Al junction the normal metal-superconductor conductance is greater than the normal conductance. Interestingly, the situation is reversed at a voltage of 0.1 mV. In contrast, for Al-CNT(4,0)-Al junction, the normalized conductance remains negative for voltages less than the superconducting gap.

IV. CONCLUSIONS AND FUTURE DIRECTION

In conclusion, we have studied Andreev reflection in normal-superconductor junctions using density functional theory based transport calculations. This approach allowed us to include the atomistic details of the

junction electronic structure in the extended Blonder-Tinkham-Klapwijk model. We studied Au-Al and Cu-Pb all metal junctions and calculated the normal and normal-superconductor conductances for different separations of the two materials at the interface. Our transverse momentum resolved analysis has allowed us to identify contributions to these quantities from different parts of the Brillouin zone. We found that the conductances for junctions in the superconducting state follows a similar k -point dependence as the normal state conductance. In other words, Andreev reflection is higher in Brillouin zone regions, where transmission is also high.

We have also investigated Co-Pb ferromagnet-superconductor junctions. In this case, while at zero bias, our results satisfactorily match the experimental reports, a discrepancy was revealed at a finite bias, particularly at voltages close to the superconductor gap. This could possibly be attributed to stray magnetic fields from the ferromagnet or to proximity effects, both causes which are not included in the extended Blonder-Tinkham-Klapwijk model.

We further studied Andreev reflection from carbon nanotubes sandwiched between normal metal and superconducting electrodes and found G_{NS}/G_N ratios to lie on opposite sides of unity for (3,0) (higher than one) and (4,0) (lesser than one) carbon nanotubes. This highlights the sensitivity of such calculations to details and the need for a truly atomistic theory for tackling this problem.

Concerning the potential outlook for future studies, our work provides a stepping stone for analyzing with first-principles methods the experimental setups needed to investigate and detect Majorana fermions. These particles, which are their own anti-particles, are expected to play a crucial role in topological quantum computing and have recently garnered significant attention in the condensed matter community. After several theoretical proposals, signatures of this particle were found experimentally in large spin-orbit nanowires in proximity with superconductors^{23,24}. However, a number of issues remain unresolved and important questions need to be answered to confirm that indeed Majoranas were observed. Our implementation of the phenomenology of Andreev reflection in a first-principles approach can be quite useful to study such a setup, in particular, by taking into account the underlying electronic structure of the nanowires. When combined with the order- N implementation of our SMEAGOL code²⁵, which allows us treating thousands of atoms, it opens the opportunity of recreating theoretically the aforementioned experiments in an *ab initio* manner, which till now have been modelled empirically.

Acknowledgments

AN is financially supported by Irish Research Council under the EMBARK initiative. IR and SS acknowledge additional support by KAUST (ACRAB project). The

computational resources have been provided by Trinity Centre for High Performance Computing.

-
- ¹ A.F. Andreev, Sov. Phys. JETP **19**, 1228 (1964).
² M. Tinkham, *Introduction to Superconductivity* (Dover, New York, 2004).
³ S.K. Upadhyay, A. Palanisami, R.N. Louie, and R.A. Buhrman, Phys. Rev. Lett. **81**, 3247 (1998).
⁴ R.J. Soulen Jr., J.M. Byers, M.S. Osofsky, B. Nadgorny, T. Ambrose, S.F. Cheng, P.R. Broussard, C.T. Tanaka, J. Nowak, J.S. Moodera, A. Barry, and J.M.D. Coey, Science **282**, 85 (1998).
⁵ F. Taddei, S. Sanvito, and C.J. Lambert, J. Low Temp. Phys. **124**, 305 (2001).
⁶ K. Xia, P.J. Kelly, G.E.W. Bauer, and I. Turek, Phys. Rev. Lett. **89**, 166603 (2002).
⁷ T.Y. Chen, Z. Tesanovic, and C.L. Chien, Phys. Rev. Lett. **109**, 146602 (2012).
⁸ M. Eschrig, A.A. Golubov, I.I. Mazin, B. Nadgorny, Y. Tanaka, O.T. Valls, and I. Zutic, Phys. Rev. Lett. **111**, 139703 (2013).
⁹ A.F. Morpurgo, J. Kong, C.M. Marcus, and H. Dai, Science **286**, 263 (1999).
¹⁰ A. Kormanyos, I. Grace, and C.J. Lambert, Phys. Rev. B **79**, 075119 (2009).
¹¹ I. Knez, R.-R. Du, and G. Sullivan, Phys. Rev. Lett. **109**, 186603 (2012).
¹² P. Adroguer, C. Grenier, D. Carpentier, J. Cayssol, P. Degiovanni and E. Orignac, Phys. Rev. B **82**, 081303(R) (2010).
¹³ Q.-F. Sun, Y.-X. Li, W. Long and J. Wang, Phys. Rev. B **83**, 115315 (2011).
¹⁴ A. Narayan and S. Sanvito, Phys. Rev. B **86**, 041104(R) (2012).
¹⁵ B. Wang, Y. Wei, and J. Wang, Phys. Rev. B **86**, 035414 (2012).
¹⁶ L.N. Oliveira, E.K.U. Gross, and W. Kohn, Phys. Rev. Lett. **60**, 2430 (1988).
¹⁷ M.J.M. de Jong and C. Beenakker, Phys. Rev. Lett. **74** 1657 (1995).
¹⁸ G.E. Blonder, M. Tinkham, and T.M. Klapwijk, Phys. Rev. B. **25**, 4515 (1982).
¹⁹ C. Beenakker, Phys. Rev. B **46** 12841 (1992).
²⁰ A. R. Rocha, V. M. Garcia-Suarez, S. Bailey, C. Lambert, J. Ferrer, and S. Sanvito, Nat. Mater. **4**, 335 (2005).
²¹ A. R. Rocha, V. M. Garcia-Suarez, S. Bailey, C. Lambert, J. Ferrer, and S. Sanvito, Phys. Rev. B **73**, 085414 (2006).
²² I. Rungger and S. Sanvito, Phys. Rev. B **78**, 035407 (2008).
²³ V. Mourik, K. Zuo, S.M. Frolov, S.R. Plissard, E.P.A.M. Bakkers, and L.P. Kouwenhoven, Science **336**, 1003 (2012).
²⁴ A. Das, Y. Ronen, Y. Most, Y. Oreg, M. Heiblum, and H. Shtrikman, Nature Physics **8**, 887 (2012).
²⁵ B. Naydenov, M. Mantega, I. Rungger, S. Sanvito and J.J. Boland, Phys. Rev. B **84**, 195321 (2011).